Numerical study of Richtmyer-Meshkov instability in finite thickness fluid layers with reshock

Linfei Li,[1] Tai Jin,[2,*] Liyong Zou,[3,†] Kun Luo,[1] and Jianren Fan[1]

[1]*State Key Laboratory of Clean Energy Utilization, Zhejiang University, Hangzhou 310027, People's Republic of China*
[2]*School of Aeronautics and Astronautics, Zhejiang University, Hangzhou 310027, People's Republic of China*
[3]*Laboratory of Shock Wave and Detonation Physics, Institute of Fluid Physics, China Academy of Engineering Physics, Mianyang 621900, People's Republic of China*

(Received 18 September 2023; accepted 23 April 2024; published 23 May 2024)

The evolution of a shock-induced fluid layer is numerically investigated in order to reveal the underlying mechanism of the Richtmyer-Meshkov instability under the effect of a reshock wave. Six different types of fluid layer are initially set up to study the effect of amplitude perturbation, fluid-layer thickness, and phase position on the reshocked fluid-layer evolution. Interface morphology results show that the interface-coupling effect gets strengthened when the fluid-layer thickness is small, which means the development of spikes and bubbles is inhibited to some extent compared to the case with large initial fluid-layer thickness. Two jets emerge on interface II_1 under out-of-phase conditions, while bubbles are generated on interface II_1 when the initial phase position is in-phase. The mixing width of the fluid layer experiences an early linear growth stage and a late nonlinear stage, between which the growth of the mixing width is considerably inhibited by the passage of the first and the second reshock and mildly weakened during phase reversion. The amplitude growth of interfaces agrees well with the theoretical model prediction, including both the linear and nonlinear stages. In the very late stage, the amplitude perturbation growth tends to differ from the theoretical prediction due to the squeezing effect and stretching effect.

DOI: 10.1103/PhysRevE.109.055105

I. INTRODUCTION

The Richtmyer-Meshkov (RM) instability, which has been proved by theoretical derivation [1] and later confirmed experimentally [2], reveals the phenomenon of a shock wave impulsively accelerating a disturbed interface that has been separated by two fluids with different densities. After the shock wave collides with the disturbed density interface, the disturbed interface obtained an instantaneous speed. Because the pressure gradient across the shock wave and the density gradient across the interface are misaligned, baroclinic vorticity deposits on the interface and subsequently initiates perturbation growth. The interface begins to perturb and evolves into characteristic structures such as bubbles and spikes, and finally transitions to turbulence. Owing to its significant role in natural and scientific fields, researchers devote much attention to the RM instability and have already conducted various research in related fields such as supernova explosions [3,4], inertial confinement fusion (ICF) [5,6], supersonic and hypersonic combustion [7,8], and others. The investigation of RM instability, which will be helpful to the understanding of underlying mechanisms and the development of related research fields, is of significance.

Studies of the RM instability first focused on the single interface-shock interaction [9–11] in order to reveal the development of the RM instability at different stages and the complicated evolution mechanisms. Later, the interactions between the fluid layer and shock waves were further investigated [12], where it was found that the evolution mechanism under the fluid layer turns out to be more complicated, and many additional effects, such as interface coupling, rarefaction wave, and compression wave effects are revealed. Jacobs *et al.* [13] investigated the evolution of a shock-induced thin fluid layer within a shock tube and observed three distinct flow patterns: a mushroom-shaped structure on the first interface, a mushroom-shaped structure on the second interface, and no mushroom-shaped features shown on the fluid layer. Prestridge *et al.* [14] performed particle image velocimetry measurements of RM instability in a thin layer accelerated by a planar shock wave, and the circulation in the curtain during the vortex-dominated, nonlinear stage of the instability evolution is presented, which are employed to validate an idealized model of the nonlinear perturbation growth. Tomkins *et al.* [15] conducted an experimental investigation of mixing mechanisms in a shock-induced instability flow. The quantitative two-dimensional concentration of the heavy gas (SF_6) was obtained and a large amount of mixing associated with the primary instability was found. Sun *et al.* [16] investigated the convergent RM instability of a SF_6 gas layer with a uniform interface outside and a sinusoidal interface inside. They revealed that the evolution of the inner interface experienced three stages and proposed an empirical model for the prediction of the growth of RM instability. Using soap film techniques, Liang *et al.* [17] designed five kinds of heavy gas layer and investigated the development of each individual interface accelerated by the planar shock waves. They found

*jintai@zju.edu.cn
†zly@caep.cn

that the reflected rarefaction waves tend to impose different effects on the gas layer when the initial perturbation on the gas layer was different and quantitatively evaluated the effect of the rarefaction waves on the evolution of the first interface. Subsequently, the light-fluid-layer evolution accelerated by the shock wave was further investigated experimentally and theoretically by Liang and Luo [18]. They found that the thickness of the fluid layer and the speed of the two interfaces eventually converged, which is due to the multiple reflected shocks reverberating inside the light fluid layer.

Recently, the study of RM instability with reshock has received further attention. Balakumar *et al.* [19] and Balasubramanian *et al.* [20] experimentally studied the fluid-layer evolution with and without reshock, the dramatic impact on the mixing, and the transition to turbulence from the reshock wave was highlighted. Leinov *et al.* [21] experimentally and numerically revealed that the evolution of the mixing zone after reshock was independent of its amplitude at the time of the reshock but dependent directly on the strength of the reshock. Sewell *et al.* [22] performed experiments on the RM instability by considering small- and large-initial-amplitude perturbations and found that the dependence of the instability growth exponent on the initial amplitude was different before and after reshock. Guo et al. [23] experimentally studied the RM instability of heavy and light interfaces by considering reshock and theoretically analyzed the linear and nonlinear growths of the mixing width of the single interface before and after reshock. The interfaces were expanded into a Fourier series with a dominant fundamental mode and more high-order modes where the fundamental mode had a predominant influence on the interface evolution after reshock. Li *et al.* [24] performed a direct numerical simulation of RM instability with reshock. It was found that rarefaction and compression waves alternatively accelerated the mixing zone after the reshock, and rarefaction waves contributed to the turbulent motions while compression waves consumed turbulent energy. Hill *et al.* [25] conducted large-eddy simulations of RM instability with reshock and the examination of the turbulent kinetic energy indicated that an expansion wave which followed reshock played a major role in driving the growth of the mixing layer. The investigations of RM instability with reshock indicate the complicated interface evolution under the reshock condition.

The thickness of the fluid layer is another important factor with a significant influence on the layer evolution. The interface-coupling effect, which tends to be prominent when a thin fluid layer is implemented, has been investigated considering the instabilities induced by rarefaction waves [17,26] and compression waves [27]. The changes in amplifications of perturbations and growth of interface when rarefaction and compression waves are involved support the idea of controlling the instability growth by rarefaction and compression waves. The fluid-layer thickness can directly impact the interface-coupling effect and further dominate the perturbation growth of interfaces. Ding *et al.* [28] experimentally studied the evolution of an air-SF_6 layer in a converging shock tube from which the relationship between the gas-layer thickness and the interface-coupling effect were analyzed. They discovered that the slow perturbation induced in the inner gas layer could be greatly suppressed by reducing the thickness of the gas layer. Cong *et al.* [29] experimentally and theoretically studied the heavy fluid layers with reshock and found that the promotion effects of the rarefaction wave on perturbation growth become weaker than the inhibition of squeezing effects when the fluid-layer thickness decreases. The acceleration stage of rarefaction waves could be well predicted by the nonlinear model by considering the effects of rarefaction waves while the interface-coupling effects were weak. Although progress has been made in the area of shock-induced fluid-layer evolution, so far the fluid-layer evolution after reshock, such as interface evolution, amplitude perturbation, and vortex field, still remains unclear and needs to be further explored.

In this work we aim to study the evolution and characteristic of the fluid layer interacting with a shock wave and subsequently the reshock wave. The effects of initial interface amplitude, phase position, and fluid-layer thickness on the fluid-layer evolution and perturbation growth are investigated. First, we presented the interface morphology of the fluid layer. Then, the quantitative analysis of the mixing widths are given. Finally, we theoretically discuss the amplitude perturbation growth, in which our simulation results and the theoretical model are compared and analyzed.

II. GOVERNING EQUATIONS AND NUMERICAL METHODS

A. Governing equations

In this study the two-dimensional unsteady conservative compressible Navier-Stokes (NS) equations considering viscosity are adopted to capture the evolution of shock waves and the density interface in the compressible flow field. The governing equations of continuity, momentum, and energy are as follows:

$$\frac{\partial \rho}{\partial t} + \frac{\partial(\rho u_i)}{\partial x_i} = 0, \tag{1}$$

$$\frac{\partial(\rho u_i)}{\partial t} + \frac{\partial[\rho u_i u_j + p\delta_{ij}]}{\partial x_j} = \frac{\partial \sigma_{ij}}{\partial x_j}, \tag{2}$$

$$\frac{\partial(\rho e_t)}{\partial t} + \frac{\partial[(\rho e_t + p)u_j]}{\partial x_j} = -\frac{\partial q_j}{\partial x_j} + \frac{\partial(u_i\sigma_{ij})}{\partial x_j}, \tag{3}$$

$$\frac{\partial(\rho Y_s)}{\partial t} + \frac{\partial(\rho Y_s u_j)}{\partial x_j} = 0, \tag{4}$$

where ρ is the fluid density, u_i ($i = 1, 2$) represents the fluid velocity in the ith direction, x_i are the spatial coordinates, p is the pressure, Y_s is the mass fraction of species s, δ_{ij} is the Kronecker delta ($\delta_{ij} = 1$ when $i = j$, $\delta_{ij} = 0$ when $i \neq j$), e_t is the total energy per unit mass, $q_j = -k\frac{\partial T}{\partial x_j}$ is the heat flux in the jth direction where k is the thermal conductivity coefficient, and σ_{ij} is the viscous stress tensor that can be given as

$$\sigma_{ij} = \mu\left(\frac{\partial u_i}{\partial x_j} + \frac{\partial u_j}{\partial x_i} - \frac{2}{3}\frac{\partial u_i}{\partial x_i}\delta_{ij}\right), \tag{5}$$

in which the dynamic viscosity μ is associated with the temperature T by the Sutherland law [30],

$$\mu = \mu_0 \times \left(\frac{T}{T_c}\right)^{1.5}\frac{T_c + T_s}{T + T_s}, \tag{6}$$

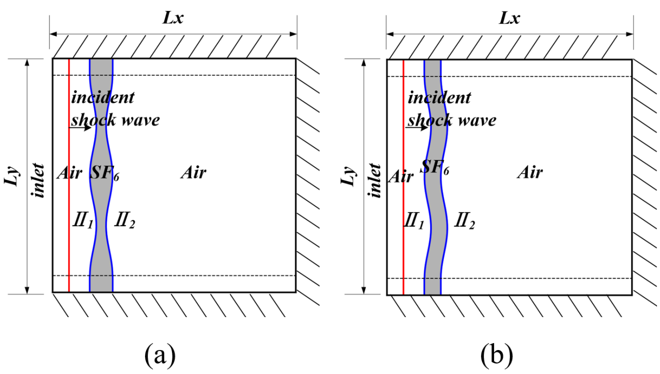

FIG. 1. Schematic of the simulation configuration: (a) the out-of-phase condition and (b) the in-phase condition. Here II_1 denotes the initial first interface and II_2 the initial second interface.

where μ_0 is the standard viscosity for gas at one standard atmospheric pressure and 0 °C, and T_c and T_s are two correlated parameters. The ideal-gas equation of state is adopted to obtain an enclosed system,

$$p = \rho \frac{R}{W} T, \tag{7}$$

where R is the molar gas constant and W is molar mass.

B. Simulation configuration

In Fig. 1 the initial numerical setup is shown. The computation domain size is set as $L_x \times L_y = 150 \times 140$ mm, which is chosen to be consistent with the experimental setup to facilitate the comparison between simulation results and the previous experiment results by Liang *et al.* [27], where the shock-accelerated SF_6 layer without reshock was measured. The initial physical parameters of the gas layer for different cases are listed in Table I. A mesh resolution of $\Delta x = 0.2$ mm and $\Delta y = 0.2$ mm, respectively, has been validated and proved to be enough for the present simulation accuracy and is then adopted. In order to capture the density interface more accurately, a 16-times refinement mesh near the initial two curved density interfaces is adopted for reducing the impact of grid sensitivity.

As sketched in Fig. 1, the single-mode perturbations as $x = 30 + a_n^0 \cos[k(y-70)+\pi]$ are imposed on the two density interfaces within the range of $y \in [10,130]$ mm, where a_n^0 (n = 1, 2) represents the initial amplitude of interfaces II_1 and II_2 and k denotes the wave number.

In the two-dimensional (2D) simulations, the incident shock wave (IS) with Mach number Ma = 1.2 is initially launched in the air region and then successively collides with the two interfaces between sulfur hexafluoride (SF_6) and air.

TABLE II. Initial conditions of the postshock and preshock states of SF_6 and air.

Quantity	Preshock Air	Postshock Air	SF_6
ρ(kg m^{-3})	1.2	1.61	5.99
p(Pa)	101300	153300	101300
T(K)	295.5	331.7	295.5
u(m s^{-1})	0.0	105.4	0.0

The preshocked ambient temperature and pressure conditions correspond to T = 295.5 K and p = 101 300 Pa, respectively. The Mach number Ma = 1.2 incident shock wave (IS) travels from left to right with a speed of 413.5 m s^{-1}; after the IS passes interfaces II_1 and II_2 consecutively, two transmitted shock waves (TS_1 and TS_2) are generated. Here, the initial Atwood number across the interface is defined as $At = (\rho_{SF_6} - \rho_{air})/(\rho_{SF_6} + \rho_{air})$, and At equals 0.67 in our present work. The initial conditions of the different section of the computational domain are listed in Table II. The initial preshock and postshock parameters (including density, pressure, temperature, and so on) are given by the Rankine-Hugoniot jump conditions:

$$\frac{p_L}{p_R} = 1 + \frac{2\gamma}{\gamma+1}(\mathrm{Ma}^2 - 1), \tag{8}$$

$$\frac{\rho_L}{\rho_R} = \frac{(\gamma+1)\,\mathrm{Ma}^2}{(\gamma-1)\,\mathrm{Ma}^2 + 2}, \tag{9}$$

$$\frac{u_L}{c_R} = \frac{1}{\gamma}\left(\frac{p_L}{p_R} - 1\right)\sqrt{\frac{\frac{2\gamma}{\gamma+1}}{\frac{p_L}{p_R} + \frac{\gamma-1}{\gamma+1}}}. \tag{10}$$

The quantities with subscript L are postshock quantities where those with subscript R represent preshock quantities.

C. Numerical schemes and validation

In the present study the numerical program BLASTFOAM [31] used is a library developed for single-phase and multiphase compressible flows based on OPENFOAM, which is suitable for high-explosive detonation, explosive safety, and air blast, as well as general compressible flows. The numerical scheme of flux adopts the HLLC approximate Riemann solver, which is used for capturing shock waves. The HLLC scheme was developed by Toro *et al.* [32] on the basis of the HLL scheme, which has a high solution accuracy for contact discontinuities. The Riemann-type flux solution is selected for solving the scalar convection term, and the second-order Runge-Kutta method is adopted for time integration. The adaptive grid refinement and CPU parallel load balancing module are coupled in the program to perform dynamic mesh

TABLE I. Initial physical parameters of SF_6 gas layer for different cases. Here a_1^0 (a_2^0) denotes the initial amplitude of the first (second) interface.

Case	AP-L10-A2	IP-L10-A2	AP-L10-A1	AP-L30-A2	IP-L30-A2	AP-L30-A1
a_1^0(mm)	2	2	1	2	2	1
a_2^0(mm)	−2	2	−1	−2	2	−1
L_0(mm)	10	10	10	30	30	30

TABLE III. Different types of grid resolution settings. BGR (base grid resolution), IRR (interface refinement ratio), ARR (adaptive refinement ratio), FGS (finest grid spacing).

Grid	BGR	IRR	ARR	FGS (μm)
A	350 × 375	1/32	1/16	12.5
B	700 × 750	1/16	1/8	12.5

refinement near the shock wave and the density interface. The numerical program BLASTFOAM has been well verified in single-phase double Mach reflection [33], shock tube–two fluid, three-phase secondary detonation, and sand-covered explosive explosions [34], which are detailed in the literature [35]. This solver has also been used to investigate the RM instability of a flat interface driven by perturbed and reflected shock waves, where the numerical results are well validated with the experimental measurement, which are detailed in our previous study [36]. In the present work the grid sensitivity is first analyzed to ensure the adequacy of the adopted mesh for the present simulation, and the numerical comparison with experimental results is further demonstrated.

1. Grid sensitivity analysis

In order to evaluate the sensitivities of simulations to the grid spacing, three different grid resolution settings are used as listed in Table III, which are the base grid spacing, the interface refinement grid spacing for the elimination of the unsmooth interface effect caused by quadrilateral mesh, and the adaptive refinement grid spacing for the capture of shock waves. The number of grid points in the streamwise direction of all base grid settings varies from 375 points (grid A) to 750 points (grid B) with the grid spacing of 12.5 μm at the finest level.

A number of comparisons of different quantities corresponding to different grids are analyzed to examine the grid sensitivities. Figure 2 shows the pressure contour of the flow field at the time of 0.7 ms when the reflected shock wave has already passed the gas layer. From the pressure contour of flow field, the characteristics of flow structure are well captured by both grids A and B. Grid B with a higher resolution reveals the flow structure of field more distinctly and vividly compared to grid A of the lower-resolution grid. Figure 3 gives the streamwise distribution of the pressure and density at $t = 0.7$ ms in flow field, and the results obtained on grids A and B are compared and proved to be fully grid converged.

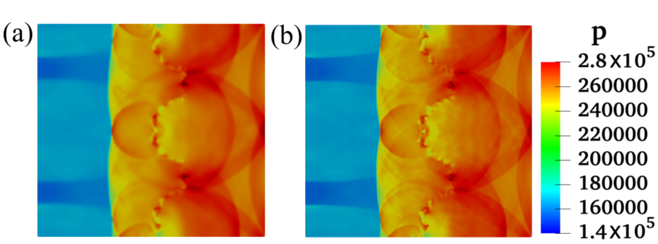

FIG. 2. Pressure contour of flow field at 0.7 ms: (a) results with the coarse mesh based on grid A and (b) results with the fine mesh based on grid B.

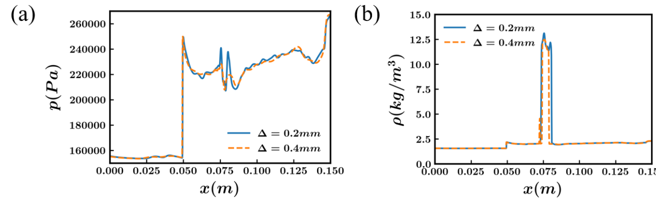

FIG. 3. Streamwise distribution of the pressure and density at 0.7 ms. Dashed orange line represents the results based on grid A, and solid blue line represents the results based on gird B.

2. Numerical validation

The schlieren of density obtained from the simulation results, which can explicitly manifest the characteristic structure of the evolution of flow field (especially the density interface), is chosen to be compared with the experimental results [27]. Figures 4 and 5 give the gas-layer evolution before reshock under out-of-phase and in-phase conditions. The phase inversion of interface II_2 has been completed before reshock, both in out-of-phase and in-phase conditions. In Fig. 4 we can see that at 67 μs, the transmitted shock wave (TS1) induced by the interaction of the incident shock wave and interface II_1 is passing through the interface II_2, and rarefaction waves and transmitted shock waves (TS2) are also generated. After the TS1 passes through interface II_2, the phase inversion of interface II_2 is completed and the two interfaces continue moving downwards. Figure 5 gives the interface evolution under in-phase conditions, in which the phase inversion of interface II_2 has been completed as well. Both the interface morphology of interface sII_1 and II_2 in Figs. 4 and 5 show good consistency with experimental results [27] in position and shape of the interfaces. Figure 6 further gives the dimensionless amplitude of interface II_1 under out-of-phase and in-phase conditions. Good consistency has been obtained in the numerical and experimental results, which verifies the accuracy of the solver used.

In addition, the solver has also been validated with experimental measurement of RM instability of a flat interface driven by perturbed and reflected shock waves in our previous work [36]. It was confirmed that the numerical results well reproduced the whole evolution process of the interactions and captured the important structures in the flow field such as spikes and bubbles. And the numerical results of the width of the mixing region were also very close to the experimental

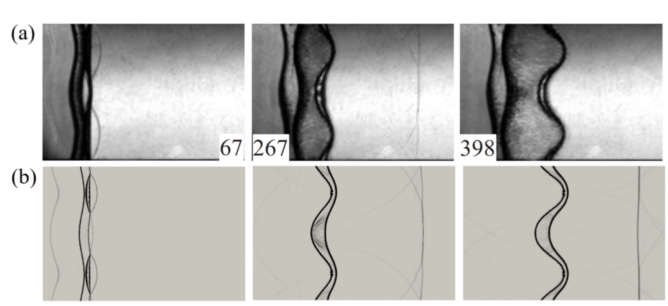

FIG. 4. Gas-layer evolution before reshock under out-of-phase conditions (in units of μs): (a) experimental and (b) numerical results.

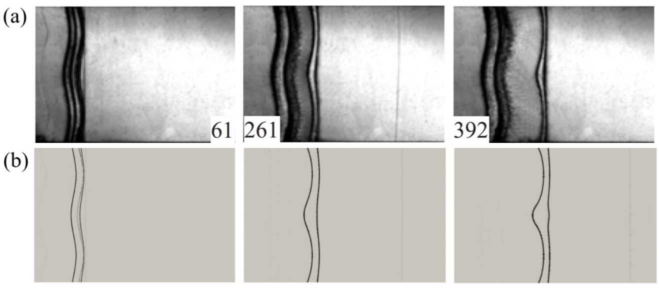

FIG. 5. Gas-layer evolution before reshock under in-phase conditions (in units of μs): (a) experimental and (b) numerical results.

measurement, which further verified the solver adopted to resolve the instability related to reshock effects.

III. RESULTS AND DISCUSSION

A. Interface morphology

Six kinds of shock-induced gas-layer evolution are simulated and analyzed, with different initial amplitudes of perturbation on the interface, phase position, and thickness of the gas layer. The initial physical parameters of the SF_6 gas layer for different cases are given in Table I. The time when the incident shock wave collides with the first interface is defined as time zero $t = 0$. From the overall density schlieren images presented in Fig. 7, it is apparent that interfaces II_1 and II_2 are evolved to typical structures, e.g., spikes, bubbles, or jets, under the impact of the reshock waves. The resulting structure is quite related to the distorted interface shape at the time of reshock arrival. This is different from the evolution of chaotic mixing layers [19–22], where they found that the perturbation growths after reshock were independent of the interface shapes at the time of reshock arrival, as discussed by Guo *et al.* [23]. In the present studied cases, the widths of the mixing layer after reshock were dramatically increased compared with those before reshock. Henry *et al.* [26] explored the RM instability of a single interface and two successive interfaces with reshock, in which spikes were being induced under the effect of reshock in the single-interface condition. Furthermore, the evolution of the successive layers of fluid is very similar to the evolution of the gas layer in the current simulation, in which jets are being induced on interface II_1 and spikes are being induced on interface II_2 under the impact of reshock.

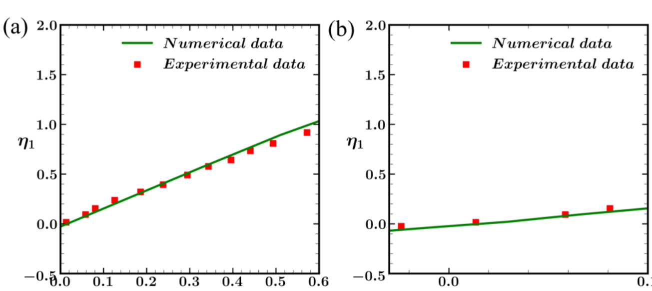

FIG. 6. Comparisons of the dimensionless amplitude of interface II_1: (a) out-of-phase (b) in-phase conditions.

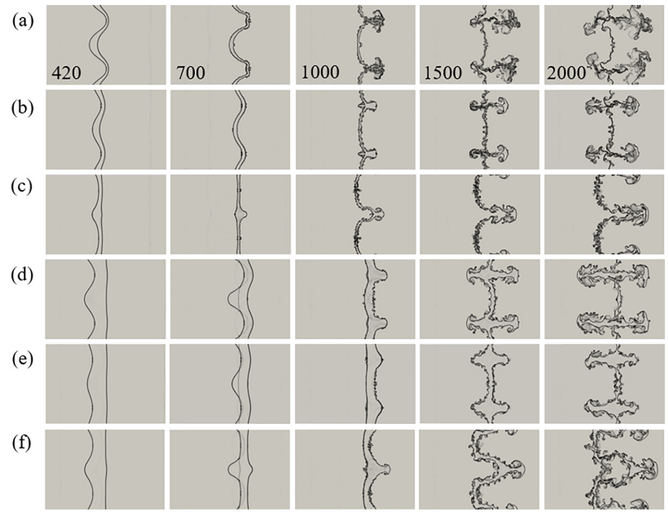

FIG. 7. Schlieren images of SF_6 gas-layer evolution in different cases (in units of μs): (a) AP-L10-A2, (b) AP-L10-A1, (c) IP-L10-A2, (d) AP-L30-A2, (e) AP-L30-A1, and (f) IP-L30-A2.

To reveal the underlying mechanism of interface evolution under different phase conditions, AP-L30-A2 (out-of-phase) and IP-L30-A2 (in-phase) cases are taken as examples. Figures 8 and 9 give the interface evolution before and after the time of the reflected shock wave passing through interface II_1 under out-of-phase conditions. From the schlieren images of the interface evolution shown in Fig. 8, obviously the planar incident shock wave first interacts with the left interface II_1, resulting in a reflected shock wave moving upstream and transmitted shock wave (TS1) with certain curvature moving downstream in the heavy gas layer, in which a positive jump velocity is given to the left interface II_1, making it move downstream. Then after the transmitted shock wave collides with the right interface II_2, a second transmitted shock (TS2) wave moving downstream is generated and a series of rarefaction waves (RW1) moving upstream in the heavy gas layer is generated as well. The right interface with certain curvature is smoothed. After a while, when the rarefaction waves interact

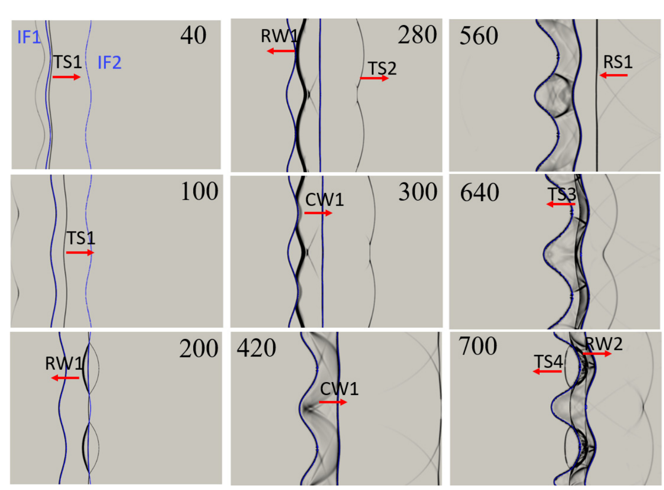

FIG. 8. Interface evolution before RS2 passes through interface II_1 under AP-L30-A2 (out-of-phase) condition (in units of μs).

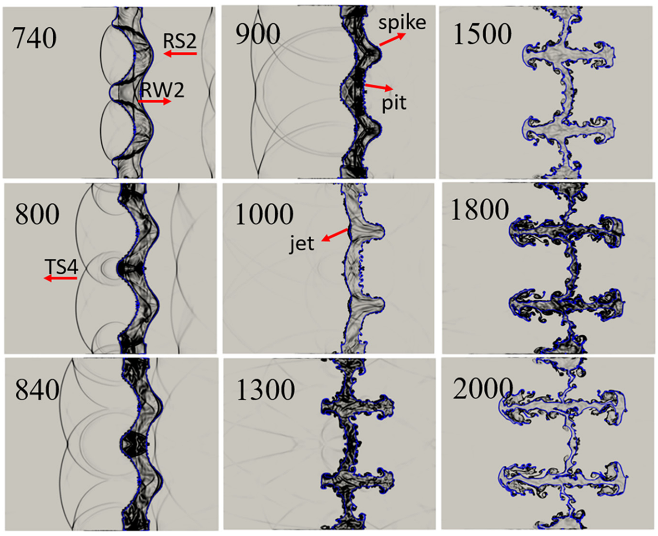

FIG. 9. Interface evolution after RS2 passes through interface II_1 under AP-L30-A2 (out-of-phase) condition (in units of μs).

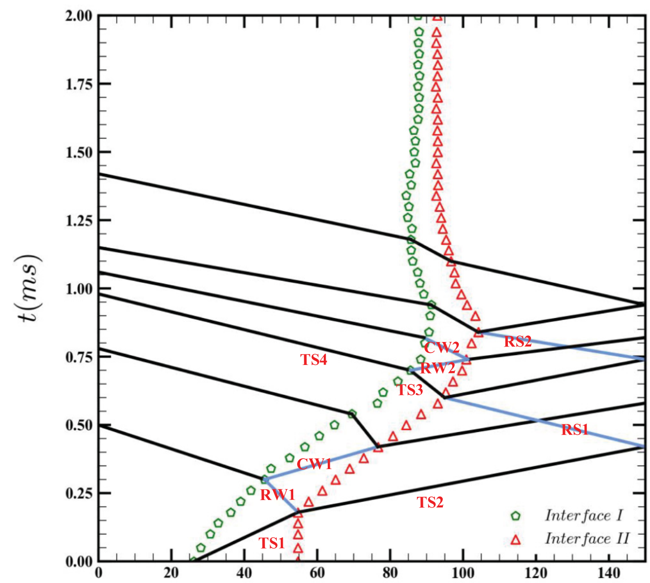

FIG. 10. Sketch of the *x*-*t* diagram for the interaction of the incident shock wave with the gas layer under AP-L30-A2. The middle position of the interface is taken as the *x* coordinate of the interface.

with the left interface, the compression waves (CW1), moving upstream in the heavy gas layer, are generated and interact with the right interface, which curves the smoothed interface. When the reflected shock wave passes through the right interface, a third transmitted shock wave (TS3) moving upstream in the heavy gas layer is generated and subsequently collides with the left interface, in which a fourth transmitted shock wave (TS4) is generated and keeps moving upstream while the generated rarefaction waves (RW2) move downstream. Figure 9 shows the interface evolution after the reflected shock wave passes through interface II_1, in which the phase inversion of interface II_1 and the development of both the two interfaces are displayed. First, when the reflected shock wave leaves interface II_1, the rarefaction waves (RW2) interact with interface II_2, increasing the curvature of interface II_2. After a while when the second reflected shock wave interacts with interface II_2, the strength of the reflected shock wave is weakened and the wave crest of interface II_2 develops gradually and changes into spike structures eventually, which is one of the most classic features of the RM instability. In addition, the collision between the third transmission shock wave (TS3) and interface II_1 leaves the vorticity deposited on interface II_1, which subsequently causes the phase inversion of interface II_1, leading to a jet formed on interface II_1. It is found that the jet on interface II_1 develops more rapidly than the spike on interface II_2. The spike structure is similar to the experimental findings by Cong et al. [29], while the jet structure is much longer in the present case, which is due to the perturbed interface II_1 used here while an unperturbed one was used in the experiments. Sketches of the motion trajectories of shock waves and interfaces accelerated by the incident shock wave are presented in Fig. 10. The middle position of the interface is taken as the *x* coordinate of the interface.

The interface evolution before and after the collision between the reflected shock wave for case IP-L30-A2 is detailed in Figs. 11 and 12. The process of the interface evolution basically contains many similarities between AP-L30-A2 (out-of-phase) and IP-L30-A2 (in-phase), which includes a series of shock-wave-interface interactions and various shock-wave generations, such as a reflected shock wave, rarefaction shock wave, and compression shock wave. Although most of the evolution process appears similar, there is much difference between two different phase initial conditions. One of the most important distinctions is that interface II_1 evolves into a spike under AP-L30-A2 (out-of-phase) condition, while interface II_1 evolves into a bubble under IP-L30-A2 (in-phase) condition. The evolution of interface in the late stage is very similar to the varicose heavy gas layer (air-SF_6-air) experiment performed by Balasubramanian *et al.* [20], in which reshock promotes the evolution of interface, resulting in an enhanced mixing and a transition to turbulence. The effect of promotion by reshock has also been manifested in the

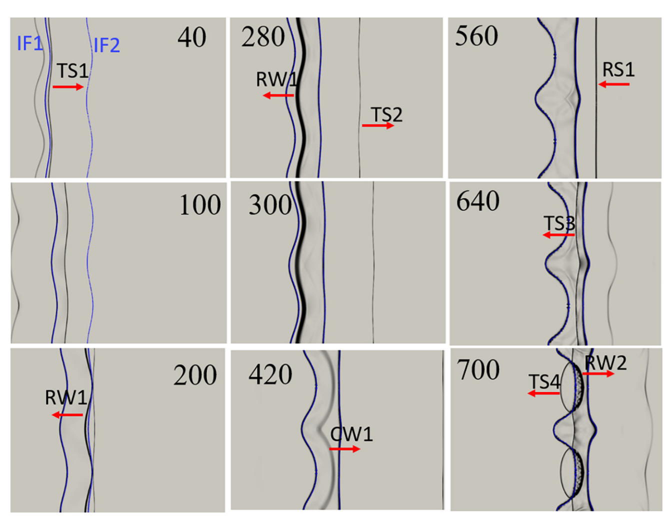

FIG. 11. Interface evolution before RS2 passes through interface II_1 under IP-L30-A2 (in-phase) condition (in units of μs).

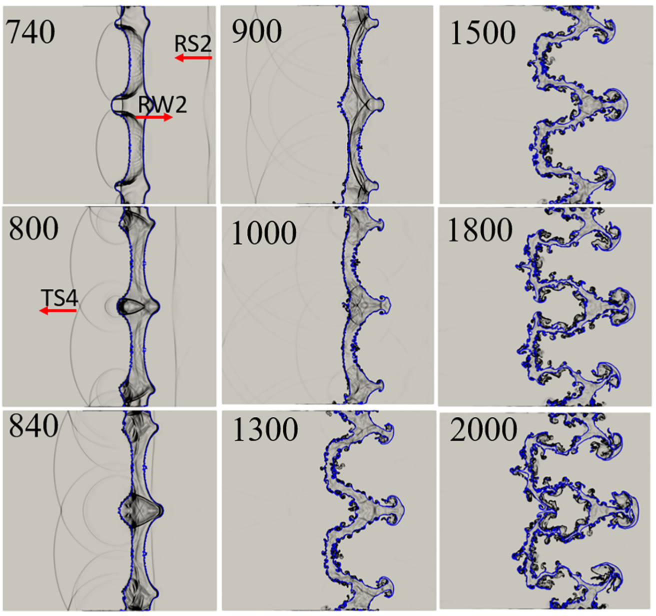

FIG. 12. Interface evolution after RS2 passes through interface II_1 under IP-L30-A2 (in-phase) condition (in units of μs).

current simulations. However, a significant difference is that the development of the interface in the experiment tends to be a more well-mixed state where the interface was heavily diffused before the arrival of the reshock.

Given that much of the subtle difference exists during the evolution process of flow field, the interface evolutions of AP-L30-A2 (out-of-phase) and IP-L30-A2 (in-phase) are compared in Figs. 13 and 14, in order to get a clearer understanding of the interface evolution under different phase conditions. Figure 13 presents the comparison of the interface evolution before the reflected shock wave interacts with interface II_1. The development of interface II_1 collectively gives an almost identical evolution process under both out-of-phase and in-phase conditions, which mainly shows that the phase of interface II_1 retains the same as the initial condition, but the width of interface II_1 increases gradually under the action of the incident shock wave and RW1. However, interface II_2 manifests a completely different phenomenon of interface evolution due to the initial differentiated phase condition. During the interaction between TS1 and interface II_2, much baroclinic vorticity is deposited on interface II_2, resulting in a progressive change mainly in the part of interface II_2 with large curvature, which nearly smooths interface II_2

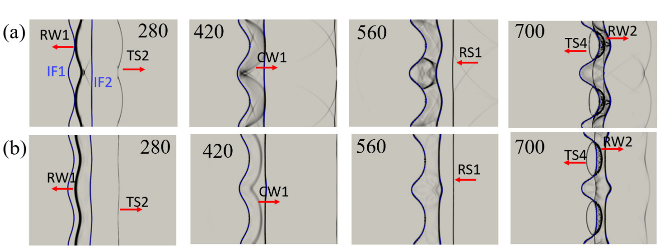

FIG. 13. Comparisons of interface evolution before RS2 leaves (in units of μs): (a) out-of-phase and (b) in-phase conditions.

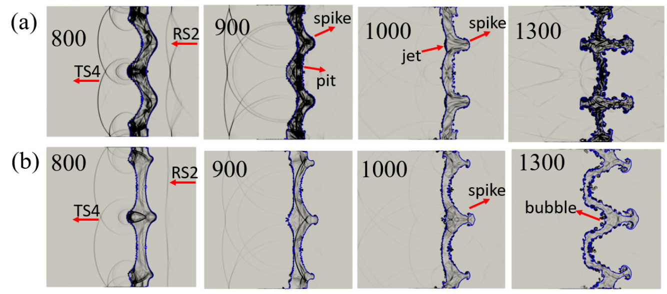

FIG. 14. Comparisons of interface evolution after RS2 leaves (in units of μs): (a) out-of-phase and (b) in-phase conditions.

to a straight line. After the transmitted shock wave passes through interface II_2, the deformation and distortion of the interface under the influence of baroclinic vorticity lead to a phase inversion of interface II_2 and continues to increase the disturbance amplitude of the interface II_2. Furthermore, after the phase reversion, the phase direction of interfaces II_1 and II_2 under the out-of-phase condition remain the same, while they remain opposite under the in-phase condition. The comparison of the interface evolution after the reflected shock wave interacts with interface II_1 is presented in Fig. 14. Following the interaction between a transmitted shock wave (TS3) and interface II_1, interface II_1 begins to experience a phase reversion while interface II_2 continues to develop nonlinearly. After the phase reversion of interface II_1 completes and the nonlinear growth of interface II_2 reaches a certain stage, interface II_1 develops jets (opposite direction to the phase of interface II_2) under the out-of-phase condition and bubbles (same direction with the phase of interface II_2) under the in-phase condition, while spikes are produced on interface II_2 owing to the continuous nonlinear growth.

The evolution of vortex under both out-of-phase and in-phase conditions is presented and compared in Fig. 15. At 2000 μs, the main classic structures of the entire evolution

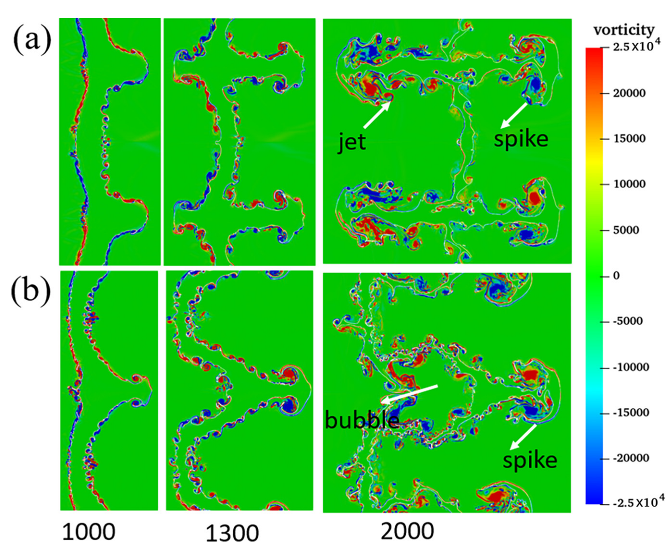

FIG. 15. Comparisons of vortex evolution under different phase conditions (in units of μs): (a) out-of-phase and (b) in-phase conditions.

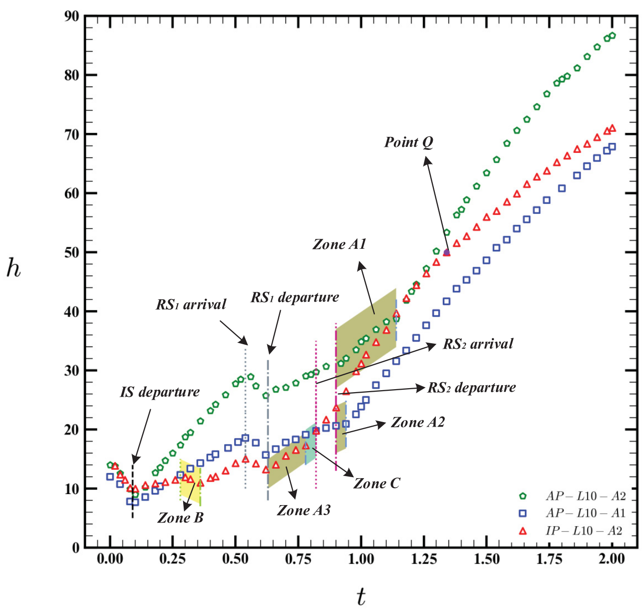

FIG. 16. Variations of the overall mixing width of gas layers vs time for the three $L_0 = 10$ mm cases (h is in units of mm, t is ms).

process, such as spikes, bubbles, and jets, show up and their shapes and specific structural features are evolved. The interface evolution under out-of-phase condition develops jets on interface II_1 and spikes on interface II_2. The development speed of jet is much faster than spike, resulting in much more vortex structures on interface II_1. The vortex structures on the pit of both interfaces are stretched and weakened for the reason of both jets and spikes' streamwise stretch. However, under in-phase conditions, interface II_1 evolves into bubbles while spikes are developed on interface II_2. The vortex of spike is shaped much like a classic mushroom structure, which is different from the vortex of bubble, presenting a nonhead mushroom structural shape. With the effect of the entrainment of vortex cores on interface II_1, the bubbles are encircled eventually.

B. Quantitative analysis of the mixing width

Figure 16 shows the variations of the overall mixing width (h) of gas layers vs time for the three $L_0 = 10$-mm cases. The overall mixing width, defined as the width between two interfaces, is measured from the leftmost bound of gas layer II_1 to the rightmost bound of gas layer II_2. According to the characteristic interface interaction periods and shock arrival time during the entire evolution process, two stages and three instants are mainly identified in order to give an intuitive and clear description of the growth of the mixing width. As displayed in Fig. 16, the initial decrease in mixing width is ascribed to the compression of incident shock wave into the gas layer, and then the mixing width begins to increase linearly after the incident shock wave completely passes interface II_2, because the jump velocity obtained by interface II_2 is higher than that of interface II_1. After a period of linear growth stage until about 0.28 ms, interface II_2 under in-phase condition starts to undergo phase inversion (zone B), leading to the decrease of the mixing width under in-phase conditions. Then, the mixing width continues to increase after the completion of phase inversion. This phenomenon of the mixing width with decrease and increase has not occurred under both the two out-of-phase conditions on account of the phase inversion when the transmitted shock wave (TS1) interacts with interface II_2, which means the mixing width keeps increasing before the arrival of the first reshock wave (RS1). The first reshock wave arrives at around 0.54 ms. During the process of the first reshock wave passing through the gas layer, the impact from the first reshock wave (RS1) imposed on interface II_2, and interface II_1 consecutively compresses the gas layer, leading to a drop in the mixing width. After the first reshock wave leaves, the mixing width under both the two out-of-phase conditions preserves a period of approximately linear growth stage until the second reshock wave arrives, while the mixing width under the in-phase condition also contains a later short-time rapid growth stage in addition to the approximately linear growth stage following the first reshock-wave departure. The difference of the mixing width between out-of-phase and in-phase conditions is ascribed to the phase inversion after the first reshock departure under the in-phase condition. After the first reshock wave completely passes through the gas layer, interface II_1 under in-phase condition begins to inverse and the phase inversion (zone A3) ends before the arrival of the second reshock wave. Following the completion of the phase inversion, a bubble emerges on interface II_1 and develops upstream, resulting in an abrupt rise in the mixing width (zone C). The mixing width growth is slightly inhibited during the second reshock wave passing through the gas layer. After the second reshock wave leaves, the mixing width under the in-phase condition increases at a remarkably amplified growth rate, while the mixing width under the two out-of-phase conditions increases slowly owing to the phase inversion of interface II_1 following the departure of the second reshock wave (zone A1 and zone A2). A jet is induced from interface II_1 subsequent to the completion of the phase inversion developing upstream, which greatly enhances the mixing width. Since there is no jet formed on interface II_1 under the in-phase condition, the relatively rapid growth rate of the mixing width is not able to be regained, resulting in the mixing width increases at a lower growth rate around the time of point Q. Interfaces II_1 and II_2 continuously keep blending together under the in-phase condition, which promotes the mixing between the two interfaces and exerts a certain amount of impact on the evolution and movement of the two interfaces, also contributing to some extent to the incapacity of increase in the mixing width at a rapid growth rate. Under the condition of the initial amplitude of interface $L_0 =$ 10 mm, the overall mixing width of the three cases is explicitly displayed in Fig. 16, from which the general trend shows that the mixing width under case (AP-L10-A2) keeps substantially higher during the entire evolution process, while cases (AP-L10-A1 and IP-L10-A2) roughly collapse, which shows that the mixing width of case (AP-L10-A1) exceeds that of case (IP-L10-A2) at the early stage and the mixing width of case (IP-L10-A2) overtakes that of case (AP-L10-A1) at the later stage. The distinguishable rise shown in case (AP-L10-A2) is ascribed to the larger initial amplitude of interface, which leads to more intense evolution of the gas layer and more rapid development of the characteristic structures such as spikes and jets, resulting in a higher mixing width. Li *et al.* [24] and Hill *et al.* [25] conducted three-dimensional simulation on the RM instability of a light or heavy interface with reshock, from which the temporal evolution of three-dimensional isosurfaces was given. The strike of reshock enhances the mixing, and the morphology of the interface becomes more broken, which bears strong resemblance to that of case AP-L10-A2 in the current simulation, exhibiting the characteristics of complete development and turbulence. The reasons for the unusual low level of the mixing width presented in case (IP-L10-A2), which remains a larger initial amplitude of interface as well, lie in the inhibition of interface amplitude on interface II_2 due to the passage of the incident shock wave (IS) and the following phase inversion. This kind of inhibition at the early stage significantly suppresses the growth in the mixing width, causing the unusual low mixing width compared to case (AP-L10-A2). The inhibition of interface II_2 of case (IP-L10-A2) between the departure of the incident shock wave (IS) and the beginning of the phase inversion lowers the mixing width quite close to case (AP-L10-A1). After the phase inversion starts, the mixing width of case (IP-L10-A2) decreases while case (AP-L10-A1) preserves a tendency towards rising, which endures until the end of the phase inversion and leads to a drop in the mixing width from case (AP-L10-A1) to case (IP-L10-A2). Since the completion of the phase inversion, the mixing width of case (IP-L10-A2) begins to increase with an almost unchanged drop of mixing width from case (AP-L10-A1) to case (IP-L10-A2). At around 0.78 ms, the phase inversion of interface II_1 is in completion and the bubble subsequently generated on interface II_1 improves the growth of the mixing width, making the mixing width of case (IP-L10-A2) nearly equivalent to case (AP-L10-A1). The mixing width of case (IP-L10-A2) overtakes that of case (AP-L10-A1) at the later stage owing to the larger growth rate caused by the emergence of the bubble.

The variations of the overall mixing width (h) of gas layers vs time for the three $L_0 = 30$ mm cases are shown in Fig. 17. Owing to the compression imposed on the gas layer when the incident shock wave passes through, the mixing width experiences a period of decrease stage and subsequently starts to increase at an approximately linear growth rate after the departure of the incident shock wave. Since the initial thickness of the gas layer ($L_0 = 30$ mm) under these three cases is much higher than the previous ($L_0 = 10$ mm), which prolongs the process of RW1 moving upstream and CW1 moving downstream in the gas layer, the time of RW1 interacting with interface II_1 and CW1 interacting with interface II_2 is delayed accordingly. From Fig. 17 we can notably see that the rarefaction waves arrive around 0.34 ms and the compression waves arrive around 0.44 ms, which is different from the previous cases with short initial thickness of the gas layer ($L_0 = 10$ mm), in which the rarefaction waves interface II_1 and the compression waves interface II_2 interaction happens around the time when the incident shock wave leaves the gas layer. The convergent RM instability of a heavy gas layer with a perturbed outer interface was experimentally studied by Ding *et al.* [28], in which the relationship between the thickness of the gas layer and the effect of the interface coupling was revealed. As the initial thickness of the gas layer increases, the interface-coupling effect decreases, leading to a slower evolution of the gas layer, which has been proved in the current simulation through the comparison of gas layers with different initial thickness. Now that RW1 and CW1 strike the interface, after a while when the incident shock wave leaves the gas layer, both the rarefaction waves and the compression waves have a great impact on the evolution of the gas layer, which reflects in the mixing width, suppressing the earlier rapid linear growth first and then accelerating the mixing width to a level close to the earlier rapid linear growth. The influence of the rarefaction waves and the compression waves is neglected under the previous case ($L_0 = 10$ mm) because of the insignificance compared to the incident shock wave under these cases. The first reshock wave arrives at around 0.58 ms. The passage of RS1 through the gas layer compresses the gas layer, reducing the mixing width to a great degree. After RS1 leaves the gas layer, the interface mixing width preserves a period of roughly linear growth stage until the second reshock wave arrives and strikes the interfaces. The growth rate of the mixing width under the in-phase condition is much higher than the two out-of-phase conditions, which is mainly attributed to the rapid development of the spike on interface II_2. Although the second rarefaction waves and the second compression waves are generated and subsequently strike the gas-layer interfaces, there is no observable oscillation shown in the mixing width, such as the major changes caused by the RW1 and CW1. The reason for the insignificant existence of RW2 and CW2 on the gas layer can be concluded as the exceeding impact of the first reshock wave than that of the RW2 and CW2. The passage of RS1 leads to a rapid evolving stage of interface II_2 and therefore an amplified growth width in the mixing width, causing the effect of RS1 to predominate the development of the mixing width and hence the subtle influence of the RW2 and CW2 can be negligible. During the period of the second reshock wave passing through the gas

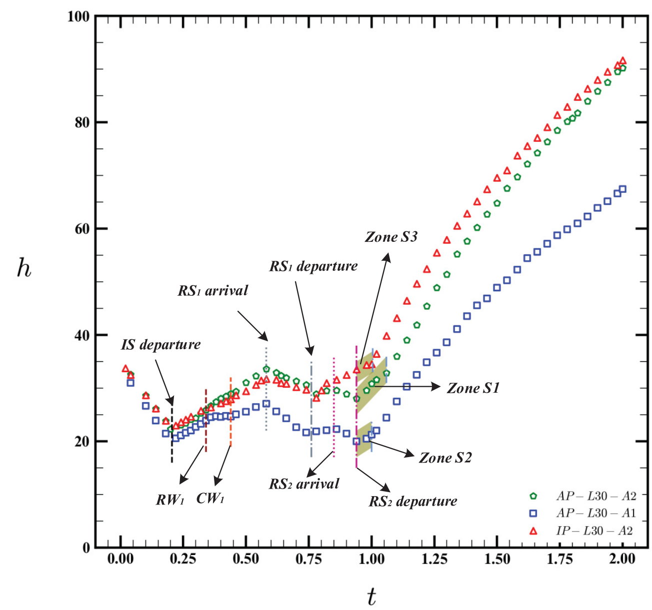

FIG. 17. Variations of the overall mixing width of gas layers vs time for the three $L_0 = 30$ mm cases (h is in units of mm, t in ms).

layer, the mixing width under the two out-of-phase conditions starts to decrease due to the compression of RS2, while the mixing width under the in-phase condition continues to increase only at a lower growth rate because of the extremely rapid growth before. Following the departure of the second reshock wave, a short period of slow growth stage in the mixing width presents under the three cases, which manifests the phase inversion of interface II_1, including zone S1 (AP-L30-A2), zone S2 (AP-L30-A1), and zone S3 (IP-L30-A2). After the completion of the phase inversion, interface II_1 under the two out-of-phase conditions generates jets, while bubbles are induced under the in-phase condition. The appearance of the bubble and jet expedites the evolution of the gas layer and greatly elevates the mixing width to a higher level, from which the mixing width under the three cases keeps increasing at a rapid growth rate. Over the whole mixing width variation under the $L_0 = 30$ mm condition, the two cases (AP-L30-A2 and IP-L30-A2) with a larger initial amplitude of interface keep a distinctly close mixing width growth during the entire evolution process, except that period of time between the departure of the first reshock wave and the emergence of the jet when the mixing width under the in-phase condition (IP-L30-A2) overtakes that of the out-of-phase condition (AP-L30-A2) for reasons of rapid development of the spike on interface II_2. The overall mixing width under case (AP-L30-A1) with a small initial amplitude of interface shows a significant difference from cases (AP-L30-A2 and IP-L30-A2), which gives a notably lower mixing width since the arrival of the first rarefaction waves. The crucial drop of case (AP-L30-A1) appearing in the interface mixing width is attributed to that the interface with a large initial amplitude is more susceptible to the shock-wave impact, which means that all kinds of shock waves induced during the entire evolution process, such as the rarefaction waves, the compression waves, and so on, have less influence on the interfaces under case (AP-L30-A1). The evolution of the gas layer under case (AP-L30-A1) is milder at the early stage, and the characteristic structures, such as the spike and the jet, cannot keep the development as rapid as cases (AP-L30-A2 and IP-L30-A2), with a larger initial amplitude of interface at the later stage. Both the inhibition of the gas layer due to a small initial amplitude of interface leaves case (AP-L30-A1) a overall lower mixing width.

C. Theoretical analysis of amplitude perturbation growth

The time-varying growths of the perturbation amplitude of interface II_1 and interface II_2 under the thicker gas layer ($L_0 = 30$ mm) are presented in Figs. 18 and 19, and the theoretical analysis of the perturbation amplitude after the incident and reshock waves are given. The nondimensional time and amplitude of interface II_1 are scaled as $\tau_1 = kv_1^l(t - t_r^*)$ and $\eta_1 = k(a_1 - a_1^*)$, with a_1^* the amplitude of interface II_1 at t_r^*, respectively, whereas the nondimensional time and amplitude of interface II_2 are scaled as $\tau_2 = k|v_2^l|(t - t_c^*)$ and $\eta_2 = k(|a_2| - |a_2^*|)$, with a_2^* the amplitude of interface II_2 at t_c^*, respectively.

Before the arrival of the reshock waves, both interface II_1 and interface II_2 undergo a linear stage, an early nonlinear stage, and a late nonlinear stage sequentially, as shown in Figs. 18 and 19. Among the three crucial stages, the growth

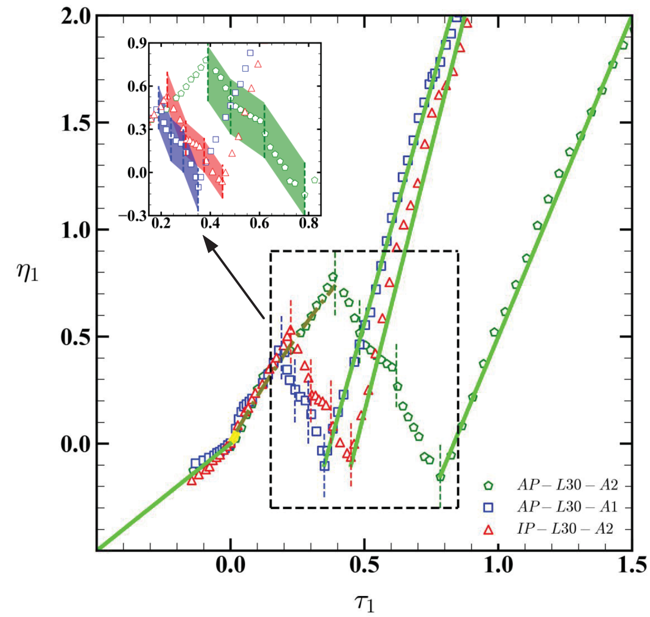

FIG. 18. Time-varying growth of the perturbation amplitude of interface II_1 under the thicker gas layer ($L_0 = 30$ mm). The green line represents the linear stage, the bold yellow line represents the early nonlinear stage [Eqs. (17)–(21)], and the dash-dot olive line represents the late nonlinear stage [Eqs. (25)–(29)].

of the interface perturbation amplitude is only dominated by the Richtmyer-Meshkov instability. Richtmyer [1] presented a linearized system of equations for the classic theoretical

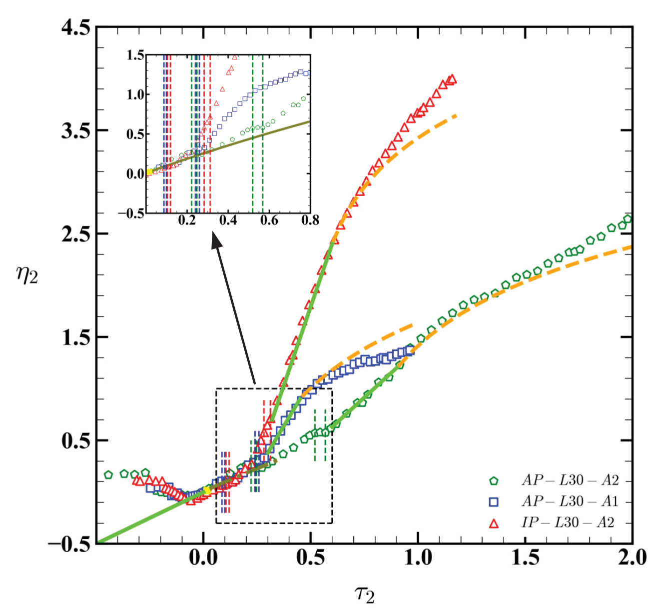

FIG. 19. Time-varying growth of the perturbation amplitude of interface II_2 under the thicker gas layer ($L_0 = 30$ mm). The green line represents the linear stage, the bold yellow line represents the early nonlinear stage [Eqs. (17)–(21)], the dash-dot olive line represents the late nonlinear stage [Eqs. (25)–(29)], and the dashed orange line represents the nonlinear stage after reshock [Eqs. (30)–(31)].

derivations. Based on that, Meyer and Blewett [37] modified the classic Richtmyer model by introducing the adoption of the average of amplitude of postshock and preshock, which gives the MB model for the prediction of the linear amplitude growth. Later, Jacobs *et al.* [38] and Mikaelian *et al.* [39] identified the importance of the interface-coupling effect on the RM instability, by which the inapplicability of the thin-layer approximation [40] can be well explained theoretically. Therefore, by considering the interface-coupling effect, a model for the prediction of the linear development of interfaces II_1 and II_2 is developed by Jacobs *et al.* [38]:

$$\frac{da_1}{dt} + \frac{da_2}{dt} = kA_t \Delta V\left(a_1^0 - a_2^0\right), \tag{11}$$

$$\frac{da_1}{dt} - \frac{da_2}{dt} = kA_c \Delta V\left(a_1^0 + a_2^0\right), \tag{12}$$

where the two modified Atwood numbers can be expressed as $A_t = \frac{\rho_2-\rho_1}{\rho_2 \tanh kh+\rho_1}$ and $A_c = \frac{\rho_2-\rho_1}{\rho_2 \coth kh+\rho_1}$.

Recently, Liang and Luo [27] modified the model developed by Jacobs *et al.* [38] on the basis of the work of Richtmyer [1] and Meyer and Blewett [37] for a better prediction of the growth of the interface perturbation amplitude, which includes the consideration of shock compression effect on the interface:

$$v_{1/2}^l = \frac{k\Delta u_1\left[A_t\left(a_1^0 - a_2^0\right) \pm A_c\left(a_1^0 + a_2^0\right)\right]}{2}. \tag{13}$$

The modified model by Liang and Luo [27] with two new modified Atwood numbers $A_t = \frac{\rho_2-\rho_1}{\rho_2 \tanh(Z_L kL_0/2)+\rho_1}$ and $A_c = \frac{\rho_2-\rho_1}{\rho_2 \coth(Z_L kL_0/2)+\rho_1}$ by introducing a new compression factor $Z_L = 1 - \Delta u_1/v_{t1}$ is shown above. The two compression factors Z_1 and Z_2 are the same as the Richtmyer impulsive theory [1] and the Meyer-Blewett impulsive theory [37], which are presented as $Z_1 = 1 - \Delta u_1/v_s$ and $Z_2 = 1 - \Delta u_2/v_{t1}$. The modified model by Liang and Luo [27] is used to compare with the simulation results, which shows a good agreement between the simulation results and the prediction value, as the green line before reshock presented in Figs. 18 and 19.

After the RW1 starts to interact with interface II_1 and the CW1 begins to interact with interface II_2, the growth of the interface perturbation amplitude enters the early nonlinear stage because of the effect RW1 imposed on interface II_1 and the effect of CW1 imposed on interface II_2. For the prediction of the early nonlinear amplitude growth, motivated by the analytical work of Mikaelian [41] and Zhang [42], Zhang and Guo (ZG) [43] gave the theoretical solution under some approximations, which is shown as follows:

$$\frac{dv}{dt} = -\alpha k\left(v^2 - v_{qs}^2\right), \tag{14}$$

with the quasi-steady velocity v_{qs} and a function of Atwood number α,

$$v_{qs}(A) = \left(\frac{Ag}{3k}\frac{8}{(1+A)(3+A)}\frac{[3+A+\sqrt{2}(1+A)^{1/2}]^2}{[4(3+A)+\sqrt{2}(9+A)(1+A)^{1/2}]}\right)^{1/2}, \tag{15}$$

$$\alpha = \frac{3}{4}\frac{(1+A)(3+A)}{[3+A+\sqrt{2}(1+A)^{1/2}]}\frac{[4(3+A)+\sqrt{2}(9+A)(1+A)^{1/2}]}{[(3+A)^2+2\sqrt{2}(3-A)(1+A)^{1/2}]}. \tag{16}$$

When RW1 interacts with interface II_1 and CW1 interacts with interface II_2, additional Rayleigh-Taylor instability (RTI) of interface II_1 and additional Rayleigh-Taylor stabilization (RTS) of interface II_2 are induced, owing to the light fluid outside the gas layer accelerating the heavy fluid inside the gas layer caused by RW1, and the heavy fluid inside the gas layer accelerating the light fluid outside the gas layer caused by CW1, respectively. Since the additional RTI of interface II_1 increases the amplitude growth rate and the additional RTS of interface II_2 decreases the amplitude growth rate [17,26], which to some extent influences the evolution of the gas layer, resulting in a more stable or unstable interface, Liang and Luo [27] modified the ZG model with consideration of the effect of the RTI of interface II_1 and the RTS of interface II_2, which is used to compare with our simulation results, showing a good agreement between the simulation results and the theoretical prediction, as the yellow line presented in Figs. 18 and 19:

$$\frac{dv_{1b/1s}^{en}}{dt} = -\alpha_{b/s}k\left[\left(v_{1b/1s}^{en}\right)^2 - \left(v_{1b/1s}^{qs}\right)^2\right], \tag{17}$$

$$\frac{dv_{2b/2s}^{en}}{dt} = \frac{a_2^0}{\left|a_2^0\right|}\alpha_{b/s}k\left[\left(v_{2b/2s}^{en}\right)^2 - \left(v_{2b/2s}^{qs}\right)^2\right], \tag{18}$$

where $v_{1b/1s}^{qs}$, $v_{2b/2s}^{qs}$, and $\alpha_{b/s}$ are calculated as follows:

$$v_{1b/1s}^{qs} = \sqrt{\frac{Ag_r}{3k}\frac{8}{(1\pm A)(3\pm A)}\frac{[3\pm A+\sqrt{2(1\pm A)}]^2}{[4(3\pm A)+\sqrt{2(1\pm A)}(9\pm A)]}}, \tag{19}$$

$$v_{2b/2s}^{qs} = \sqrt{\frac{Ag_c}{3k}\frac{8}{(1\pm A)(3\pm A)}\frac{[3\pm A+\sqrt{2(1\pm A)}]^2}{[4(3\pm A)+\sqrt{2(1\pm A)}(9\pm A)]}}, \tag{20}$$

$$\alpha_{b/s} = \frac{3}{4}\frac{(1\pm A)(3\pm A)}{[3\pm A+\sqrt{2(1\pm A)}]}\frac{[4(3\pm A)+\sqrt{2(1\pm A)}(9\pm A)]}{[\sqrt{3\pm A}+2\sqrt{2(1\pm A)}(3\mp A)]}. \tag{21}$$

After RW1 and the CW1 leave the gas layer, the evolution of the interface returns to the state of being solely dominated by RM instability. However, with the development of the gas layer, the large-amplitude effect plays a crucial role on the evolution of the interface, which indicates the small-amplitude prerequisite is not qualified owing to the large amplitude of the interfaces. Therefore the linear theory is not applicable, since the amplitude growth of the interface appears to be a trend of nonlinear development. For the prediction of the late nonlinear stage of amplitude growth, different empirical models have been proposed, including the Mikaelian (MIK) model [41,44], which found the analytical solution for both bubbles and spikes, the Sadot-Erez-Alon (SEA) model [45], which introduced a spike acceleration but failed at large kh_0, or the Zhang-Sohn (ZS) model [46,47], which captured the reduction well but had a too strong kh_0 variation. Based on these works, Dimonte and Ramaprabhu [48] introduced their new empirical model (DR model), which is applicable to a wide variety of $|A|$ and kh_0. V_0, corrected by Dimonte and Ramaprabhu, represents the interface growth rate for the condition of large amplitude, $V_0 = \frac{V_{\rm linear}}{1+(ka_0/3)^{4/3}}$, where the linear model growth rate $V_{\rm linear}$ takes the growth rate in the MB model as the initial linear growth rate,

$$V_{\rm bu/sp} = V_o \frac{1 + (1 \mp |A|)\tau}{1 + C_{\rm bu/sp}\tau + (1 \mp |A|)F_{\rm bu/sp}\tau^2}, \tag{22}$$

with coefficients $C_{\rm bu/sp}$ and $F_{\rm bu/sp}$,

$$C_{\rm bu/sp} \equiv \frac{4.5 \pm |A| + (2 \mp |A|)|kh_o|}{4}, \tag{23}$$

$$F_{\rm bu/sp} = 1 \pm |A|. \tag{24}$$

Lately, Liang and Luo [27] modified the DR model, considering various amplitude-wavelength ratios and density ratios in the late nonlinear stage:

$$v_{1b/1s}^{ln} = \frac{v_{1b/1s}^{+}[1+(1\mp A)kv_{1b/1s}^{+}t]}{1+C_{1b/1s}kv_{1b/1s}^{+}t+(1\mp A)F_{b/s}(kv_{1b/1s}^{+}t)^2}, \tag{25}$$

$$v_{2b/2s}^{ln} = \frac{v_{2b/2s}^{+}[1+(1\mp A)k|v_{2b/2s}^{+}|t]}{1+C_{2b/2s}k|v_{2b/2s}^{+}|t+(1\mp A)F_{b/s}(k|v_{2b/2s}^{+}|t)^2}, \tag{26}$$

with coefficients $C_{1b/1s}$, $C_{2b/2s}$, and $F_{b/s}$:

$$C_{1b/1s} = \frac{4.5\pm A+(2\mp A)ka_{1b/1s}^{+}}{4}, \tag{27}$$

$$C_{2b/2s} = \frac{4.5\pm A+(2\mp A)k|a_{2b/2s}^{+}|}{4}, \tag{28}$$

$$F_{b/s} = 1 \pm A. \tag{29}$$

This modified DR model is chosen to compare with our simulation results and obtains a good agreement, shown by the purple line presented in Figs. 18 and 19.

After the arrival of the first reshock wave and before the departure of the second reshock wave, there is a stage where the interface amplitude growth experiences two periods of inhibition caused by the compression of RS1 and RS2. The amplitude growth of interface II_1 as displayed in the Fig. 18 gives the evolution process inhibited by the two reshock waves. The interface amplitude growth rate begins to decrease at a relatively fast speed during RS1 and RS2 colliding interface II_1 owing to the interface compression caused by the passage of RS1 and RS2. The amplitude growth of interface II_2 as displayed in Fig. 19 shows that the amplitude growth rate increases at a relatively slow speed during the passage of RS1 and RS2 and increases at a relatively fast speed in the period after the departure of RS1 and before the arrival of RS2. The increase of the amplitude growth, although the passage of RS1 and RS2 compresses the interface, is mainly ascribed to the spike formed on interface II_2. The spike on interface II_2 ensures fast development of interface II_2, and no phase inversion occurs in this period; therefore the compression effect caused by the passage of RS1 and RS2 only inhibits interface II_2 evolution, which is not enough to reverse the increasing trend. Eventually, the amplitude growth of interface II_2 is still able to maintain an increase, while the amplitude growth of interface II_1 shows a decreasing trend for reasons of phase inversion.

After RS2 leaves, RM instability plays a dominant role in the amplitude growth. The amplitude growth of interface II_1 enters a linear stage and lasts until the end of the computational time. The amplitude growth of interface II_2 first experiences a linear stage and subsequently enters the nonlinear stage. For the prediction of the nonlinear amplitude growth, Zhang and Guo [42] take the limit g → 0 in Eq. (14) and obtain

$$\frac{dv}{dt} = -\alpha k v^2, \tag{30}$$

and they give the matched solution

$$v = \frac{v_0}{1+\alpha k v_0 t}. \tag{31}$$

The simulation results agree well with the ZG model in the early period of the nonlinear stage. But the difference appears shortly, where the ZG model underestimates the nonlinear amplitude growth in the two large initial interface amplitude ($a = 2$ mm) and overestimates the interface amplitude growth in the small initial interface amplitude ($a = 1$ mm). The overestimated prediction in the small-initial-amplitude case (AP-L30-A1) can be ascribed to the inhibition of the interface amplitude growth resulting from the squeezing effect. The squeezing effect counteracts the rarefaction wave effect on the amplitude growth and becomes increasingly strong with time. Therefore, in the small-initial-amplitude case (AP-L30-A1), the ZG model overestimates the amplitude growth since the squeezing effect is not considered in the ZG model. The two large-initial-amplitude cases (AP-L30-A2 and IP-L30-A2) exceed the prediction of the ZG model in the late period of the nonlinear stage. The reason for the underestimation of the amplitude growth can be attributed to the stronger stretching effect caused by the interaction between the interface with a large initial amplitude and the second shock wave. The large initial amplitude advances the perturbation and evolution of interface II_2, resulting in an interface with more fully developed spikes and bubbles compared to the small initial amplitude. Therefore, in the late period of the nonlinear stage, the prediction of the ZG model underestimate the interface amplitude growth, as shown by the orange line presented in Fig. 19.

IV. CONCLUSIONS

In this work the evolution of shock-induced fluid layers is numerically investigated to reveal the underlying mechanism of instability subjected to shock waves and reshock waves. Six kinds of fluid layer are initially designed to explore the effect of amplitude perturbation, fluid-layer thickness, and phase position on the fluid-layer evolution.

The interface morphology shows that the incident shock wave passes through the gas layer, accelerating the evolution of interfaces, after which spikes emerge on interface II_2. The numerical interface evolution in the early stage gives good agreement with the experimental results, in which interface II_1 maintains the phase unchanged while interface II_2 undergoes phase inversion. Furthermore, the interface morphology of interfaces II_1 and II_2 in the early stage is comparatively close to the experimental results in position and shape of the interfaces. Under the out-of-phase condition, reshock waves collide with the gas layer and phase inversion begins, leading to jets generated on interface II_1. The subsequently generated jets on interface II_1 develop more rapidly than the spikes formed on interface II_2. Under in-phase conditions, bubbles emerge on interface II_1. The bubbles under thin fluid-layer thickness evolve slowly because of the interface-coupling effect, which makes the interfaces coalesce and thus inhibits the development of the bubbles. The results indicate a strong interface shape dependence of mixing width growths and interface structures, which is similar to the experimental findings of [23,29], while the perturbation growths after reshock are found to be independent of the interface shapes at the time of reshock arrival in previous experiments [19–21].

The mixing width first experiences a decrease due to the compression of the incident shock wave passing through the gas layer. After the decrease, the mixing width undergoes both the early linear stage and late nonlinear stage, between which the first and the second reshock waves pass through the gas layer and inhibit the mixing width growth. Since the strength of the second reshock wave is much weaker than the first reshock wave, the inhibition imposed on the development of the gas layer becomes less significant, which is not enough to force the mixing width to decrease like that impacted by the first reshock wave. When a thin fluid-layer thickness is adopted, and the interface-coupling effect becomes crucial, which has a great impact on the evolution of interface II_1, making a shorter duration of the rapid growth of mixing width.

The amplitude perturbation growth of interfaces agrees well with the theoretical model prediction, including both the linear stage and nonlinear stage. Before the reshock wave arrives, both interface II_1 and interface II_2 undergo a linear stage (when the interface amplitude is only dominated by RM instability), an early nonlinear stage (when RW1 and CW1 start to have an impact on the interface evolution), and a late nonlinear stage (when the large-amplitude effect plays a crucial role on the evolution of the interface) sequentially, which had also been observed in the experiment. Additionally, the comparison of the amplitude perturbation growth between the experiment and simulation is highly desirable, in which both the experimental and numerical results are very close to theoretical prediction. However, since the experiment only explores the interface evolution without reshock, the amplitude growth with the effect of reshock, which is completely different from the growth before reshock, is not revealed in the experiment. Here, we present the amplitude perturbation growth after reshock from simulation. The passage of the first reshock and the second reshock compresses the gas layer and inhibits the development of the gas layer. However, interface II_1 decreases while interface II_2 continues to increase, which is ascribed to the spikes formed on interface II_2. After the departure of the second reshock wave, interface II_1 enters a linear stage and lasts until the end, while interface II_2 experiences a linear stage and a subsequent nonlinear stage. In the very late nonlinear stage, the amplitude perturbation growth of interface II_2 tends to differ from the theoretical prediction due to the squeezing and stretching effects.

ACKNOWLEDGMENTS

This work was supported by the National Natural Science Foundation of China (No. 52076194, No. 92052108, and No. 91952205). Support from the Laboratory of Shock Wave and Detonation Physics (No. 2021JCJQLB05704) is also acknowledged. T.J. also acknowledges financial support by Zhejiang Provincial Natural Science Foundation (No. R24E060001).

[1] R. D. Richtmyer, Taylor instability in shock acceleration of compressible fluids, Commun. Pure Appl. Math. **13**, 297 (1960).

[2] E. E. Meshkov, Instability of the interface of two gases accelerated by a shock wave, Fluid Dyn. **4**, 101 (1972).

[3] W. D. Arnett, J. N. Bahcall, R. P. Kirshner, and S. E. Woosley, Supernova 1987a, Annu. Rev. Astron. Astrophys. **27**, 629 (1989).

[4] J. Shimoda, T. Inoue, Y. Ohira, R. Yamazaki, A. Bamba, and J. Vink, On cosmic-ray production efficiency at supernova remnant shocks propagating into realistic diffuse interstellar medium, Astrophys. J. **803**, 98 (2015).

[5] M. H. Anderson, B. P. Puranik, J. G. Oakley, P. W. Brooks, and R. Bonazza, Shock tube investigation of hydrodynamic issues related to inertial confinement fusion, Shock Waves **10**, 377 (2000).

[6] J. Lindl, O. Landen, J. Edwards, and E. Moses, Review of the national ignition campaign 2009-2012, Phys. Plasmas **21**, 020501 (2014).

[7] P. Li, J. S. Bai, T. Wang, and L. Y. Zou, Large eddy simulation of a shocked gas cylinder instability induced turbulence, Sci. China Phys. Mech. Astron. **53**, 262 (2010).

[8] J. Yang, T. Kubota, and E. E. Zukoski, Applications of shock-induced mixing to supersonic combustion, AIAA J. **31**, 854 (1993).

[9] R. Ishizaki, K. Nishihara, H. Sakagami, and Y. Ueshima, Instability of a contact surface driven by a nonuniform shock wave, Phys. Rev. E **53**, R5592 (1996).

[10] J. W. Jacobs and V. V. Krivets, Experiments on the late-time development of single-mode Richtmyer-Meshkov instability, Phys. Fluids **17**, 034105 (2005).

[11] X. Guo, Z. Zhai, J. Ding, T. Si, and X. Luo, Effects of transverse shock waves on early evolution of multi-mode chevron interface, Phys. Fluids **32**, 106101 (2020).

[12] G. I. Taylor, The instability of liquid surfaces when accelerated in a direction perpendicular to their planes, I., Proc. Roy. Soc. A **201**, 192 (1950).

[13] J. W. Jacobs, D. L. Klein, D. G. Jenkins, and R. F. Benjamin, Instability growth patterns of a shock-accelerated thin fluid layer, Phys. Rev. Lett. **70**, 583 (1993).

[14] K. Prestridge, P. Vorobieff, P. M. Rightley, and R. F. Benjamin, Validation of an instability growth model using particle image velocimetry measurements, Phys. Rev. Lett. **84**, 4353 (2000).

[15] C. Tomkins, S. Kumar, G. Orlicz, and K. Prestridge, An experimental investigation of mixing mechanisms in shock-accelerated flow, J. Fluid Mech. **611**, 131 (2008).

[16] R. Sun, J. Ding, Z. Zhai, T. Si, and X. Luo, Convergent Richtmyer-Meshkov instability of heavy gas layer with perturbed inner surface, J. Fluid Mech. **902**, A3 (2020).

[17] Y. Liang, L. Liu, Z. Zhai, T. Si, and C.-Y. Wen, Evolution of shock-accelerated heavy gas layer, J. Fluid Mech. **886**, A7 (2020).

[18] Y. Liang and X. Luo, On shock-induced light-fluid-layer evolution, J. Fluid Mech. **933**, A10 (2022).

[19] B. J. Balakumar, G. C. Orlicz, C. D. Tomkins, and K. P. Prestridge, Simultaneous particle-image velocimetry-planar laser-induced fluorescence measurements of Richtmyer-Meshkov instability growth in a gas curtain with and without reshock, Phys. Fluids **20**, 124103 (2008).

[20] S. Balasubramanian, G. C. Orlicz, K. P. Prestridge, and B. J. Balakumar, Experimental study of initial condition dependence

on Richtmyer-Meshkov instability in the presence of reshock, Phys. Fluids **24**, 034103 (2012).
[21] E. Leinov, G. Malamud, Y. Elbaz, L. A. Levin, G. Ben-dor, D. Shvarts, and O. Sadot, Experimental and numerical investigation of the Richtmyer-Meshkov instability under re-shock conditions, J. Fluid Mech. **626**, 449 (2009).
[22] E. G. Sewell, K. J. Ferguson, V. V. Krivets, and J. W. Jacobs, Time-resolved particle image velocimetry measurements of the turbulent Richtmyer-Meshkov instability, J. Fluid Mech. **917**, A41 (2021).
[23] X. Guo, Z. Cong, T. Si, and X. Luo, Shock-tube studies of single and quasi-single mode perturbation growth in Richtmyer-Meshkov flows with reshock, J. Fluid Mech. **941**, A65 (2022).
[24] H. Li, Z. He, Y. Zhang, and B. Tian, On the role of rarefaction/compression waves in Richtmyer-Meshkov instability with reshock, Phys. Fluids **31**, 054102 (2019).
[25] D. J. Hill, C. Pantano, and D. I. Pullin, Large-eddy simulation and multiscale modelling of a Richtmyer-Meshkov instability with reshock, J. Fluid Mech. **557**, 29 (2006).
[26] M. T. Henry De Frahan, P. Movahed, and E. Johnsen, Numerical simulations of a shock interacting with successive interfaces using the discontinuous Galerkin method: The multilayered Richtmyer-Meshkov and Rayleigh instabilities, Shock Waves **25**, 329 (2015).
[27] Y. Liang and X. Luo, On shock-induced heavy-fluid-layer evolution, J. Fluid Mech. **920**, A13 (2021).
[28] J. Ding, J. Li, R. Sun, Z. Zhai, and X. Luo, Convergent Richtmyer-Meshkov instability of a heavy gas layer with perturbed outer interface, J. Fluid Mech. **878**, 277 (2019).
[29] Z. Cong, X. Guo, T. Si, and X. Luo, Experimental and theoretical studies on heavy fluid layers with reshock, Phys. Fluids **34**, 104108 (2022).
[30] W. Sutherland, LII. The viscosity of gases and molecular force, Lond. Edinb. Dublin Philos. Mag. J. Sci. **36**, 507 (1893).
[31] BlastFoam: A solver for compressible multi-fluid flow with application to high-explosive detonation (2020).
[32] E. F. Toro, M. Spruce, and W. Speares, Restoration of the contact surface in the "HLL-Riemann" solver, Shock waves **4**, 25 (1994).
[33] P. Woodward and P. Colella, The numerical simulation of two-dimensional fluid flow with strong shocks, J. Comput. Phys. **54**, 115 (1984).
[34] H. W. Zheng, C. Shu, Y. T. Chew, and N. Qin, A solution adaptive simulation of compressible multi-fluid flows with general equation of state, Int. J. Numer. Meth. Fluids **67**, 616 (2011).
[35] S. A. Technologies, ed., *BlastFoam Theory and User Guide* (Synthetik Applied Technologies, 2021)
[36] L. Li, T. Jin, L. Zou, K. Luo, and J. Fan, Numerical study of Richtmyer-Meshkov instability of a flat interface driven by perturbed and reflected shock waves, Phys. Fluids **35**, 026104 (2023).
[37] K. A. Meyer and P. J. Blewett, Numerical investigation of the stability of a shock-accelerated interface between two fluids, Phys. Fluids **15**, 753 (1972).
[38] J. W. Jacobs, D. G. Jenkins, D. L. Klein, and R. F. Benjamin, Nonlinear growth of the shock-accelerated instability of a thin fluid layer, J. Fluid Mech. **295**, 23 (1995).
[39] K. O. Mikaelian, Numerical simulations of Richtmyer-Meshkov instabilities in finite thickness fluid layers, Phys. Fluids **8**, 1269 (1996).
[40] E. Ott, Nonlinear Evolution of the Rayleigh-Taylor instability of a thin layer, Phys. Rev. Lett. **29**, 1429 (1972).
[41] K. O. Mikaelian, Analytic approach to nonlinear Rayleigh-Taylor and Richtmyer-Meshkov instabilities, Phys. Rev. Lett. **80**, 508 (1998).
[42] Q. Zhang, Analytical solutions of Layzer-type approach to unstable interfacial fluid mixing, Phys. Rev. Lett. **81**, 3391 (1998).
[43] Q. Zhang and W. Guo, Universality of finger growth in two-dimensional Rayleigh-Taylor and Richtmyer-Meshkov instabilities with all density ratios, J. Fluid Mech. **786**, 47 (2016).
[44] K. O. Mikaelian, Explicit expressions for the evolution of single-mode Rayleigh-Taylor and Richtmyer-Meshkov instabilities at arbitrary Atwood numbers, Phys. Rev. E **67**, 026319 (2003).
[45] O. Sadot, L. Erez, U. Alon, D. Oron, L. A. Levin, G. Erez, G. Ben-Dor, and D. Shvarts, Study of nonlinear evolution of single-mode and two-bubble interaction under Richtmyer-Meshkov instability, Phys. Rev. Lett. **80**, 1654 (1998).
[46] Q. Zhang and S.-I. Sohn, An analytical nonlinear theory of Richtmyer-Meshkov instability, Phys. Lett. A **212**, 149 (1996).
[47] Q. Zhang and S.-I. Sohn, Nonlinear theory of unstable fluid mixing driven by shock wave, Phys. Fluids **9**, 1106 (1997).
[48] G. Dimonte and P. Ramaprabhu, Simulations and model of the nonlinear Richtmyer-Meshkov instability, Phys. Fluids **22**, 014104 (2010).